COMMUN. MATH. SCI.
Vol. 17, No. 5, pp. 1437–1458

COARSE-GRAINED DESCRIPTIONS OF OSCILLATIONS IN NEURONAL NETWORK MODELS*

JENNIFER CRODELLE†, KATHERINE A. NEWHALL‡,
PAMELA B. PYZZA§, AND GREGOR KOVAČIČ¶

In memory of Professor David Shenou Cai

Abstract. Synchronous neuronal network oscillations are a ubiquitous phenomenon with great complexity of manifestations. We focus on coupled point-neuron models with increasing complexity to explore the similarities and differences in the underlying network mechanisms producing synchronous oscillations. Using simulations and coarse-grained descriptions, we illuminate mechanisms or mathematical structures that may be responsible for three stages of synchronous oscillations in the presence of noise: subthreshold dynamics, initiating a firing event, and synchronous termination of the event.

Keywords. neuronal network; integrate-and-fire; Hodgkin-Huxley; synchrony; oscillations; bifurcation; stochastic dynamics.

AMS subject classifications. 92B25; 82C31; 37N25; 37G15.

1. Introduction

Neuronal networks exhibit synchronized, oscillatory behavior occurring within and across several regions in the brain, from sensory areas such as the visual and olfactory cortex to higher-level processing centers such as the hippocampus and prefrontal cortex [11,74]. These oscillations can occur at many frequencies, reflecting a wide variability in the time scale of communication between neurons, as well as in the integration time scales within a single neuron [3,5,6,15,21,29,33,39,65,67]. Changes in properties of oscillations often underlie neurological disorders, motivating a necessity in understanding the mechanisms that give rise to oscillations occurring in a normally-functioning brain [28,79].

In this work, we study the emergence of oscillatory behavior in a variety of neuronal network models. Together with detailed network models, following the philosophy of our late mentor and friend David Cai [58], we propose possible parsimonious mechanisms underlying the network dynamics that give rise to these synchronous oscillations. In particular, we use ideas from kinetic theory and Fokker-Planck equations [12,13,32,48], firing rate networks [12,62,70], and reduction of Hodgkin-Huxley (HH) neuron models to integrate-and-fire (I&F) neuron models [1,22,31] to coarse-grain the dynamics, leaving a minimal, yet sufficient, model that explains the underlying mechanism or mathematical structure.

The remainder of the paper is organized as follows. We begin in Section 2 with an event-driven all-excitatory current-based I&F model that analyzes how quasi-periodic behavior can arise in such a network. Then, in Section 3, we introduce a conductance-based I&F model including both excitatory and inhibitory neurons, with an additional

*Received: April 23, 2019; Accepted (in revised form): September 5, 2019.
†Courant Institute of Mathematical Sciences, New York University, New York, USA (crodelle@cims.nyu.edu).
‡Department of Mathematics, University of North Carolina Chapel Hill, Chapel Hill, North Carolina, USA (knewhall@unc.edu).
§Mathematics and Computer Science Department, Ohio Wesleyan University, Delaware, Ohio, USA (pbpyzza@owu.edu).
¶Mathematical Sciences Department, Rensselaer Polytechnic Institute, Troy, New York 12180, USA (kovacg@rpi.edu).

inhibitory timescale reflecting calcium dynamics in the insect olfactory bulb. In this model, we show how the interaction of excitation and inhibition (PING) can lead to oscillatory behavior, with a slow inhibitory conductance modulating the frequency of the oscillations. Finally, in Section 4, we describe a conductance-based HH model of the prefrontal cortex, containing both excitatory and inhibitory neurons, as well as electrical coupling through gap junctions. Using this model, we show that gap-junction coupling among inhibitory neurons can initiate and sustain synchronized oscillations in a mean-dominated regime. Section 5 contains a discussion of the similarities and differences between such mechanisms across the different neuron models.

2. I&F excitatory network

Neuronal networks consisting of all excitatory neurons are ubiquitous in the developing cortex and have been shown to exhibit synchronous oscillations, usually through bursting, which are essential for normal development of cortical circuitry [21, 46, 50, 72, 73]. These bursts tend to emerge from a quiescent state and are believed to be quenched by a refractory period caused by either synaptic depression [73] or an adaptation current [46, 72], resulting in a cascade of neuronal firing followed by a period of silence.

Using the simplistic current-based I&F neuron model [10, 71], we demonstrate that a network of excitatory neurons with instantaneous synaptic connectivity is capable of producing synchronous cascades of spiking activity. These cascades of activity can occur regularly or sporadically in time depending on the magnitude of the fluctuations in the external drive. Using such a simple model allows us to analytically describe the mechanism underlying the emergence of each cascading event in the presence of noise [47–49]. Also, we calculate the time between cascading events, or network firing rate, and propose a mechanism underlying the maintenance of regularly-repeated synchronized firing events, or oscillations, in the all-excitatory network.

2.1. Model: Current-based I&F neurons. The I&F network of N excitatory neurons is governed by the following system of differential equations

$$\frac{dv_i}{dt} = -g_L(v_i - V_R) + I_i(t), \qquad i = 1, \ldots, N, \tag{2.1a}$$

where v_i is the membrane potential of the i^{th} neuron, g_L is the leakage conductance, V_R is the resting voltage, and $I_i(t)$ is the injected current. The voltage v_i evolves according to Equation (2.1a) for values below the firing threshold, V_T. When v_i reaches V_T, the i^{th} neuron is recorded to have spiked and v_i is reset to V_R. In this work, note that we use the non-dimensional values $V_R = 0$, $V_T = 1$ and $g_L = 1$.

The currents appearing in Equation (2.1a) are modeled by the expression

$$I_i(t) = f \sum_l \delta(t - s_{il}) + \frac{S}{N} \sum_{j \neq i} \sum_k A_{ji} \delta(t - \tau_{jk}), \tag{2.1b}$$

where $\delta(\cdot)$ is the Dirac delta function. The first term in Equation (2.1b) describes the current due to spikes arriving from an external source. These external spikes are modeled such that the receiving neuron's voltage is increased by an amount f at each spike time $t = s_{il}$, where the spike times are generated by a Poisson spike train with rate ν. The second term in Equation (2.1b) corresponds to the current received by the i^{th} neuron from all other network neurons $j \neq i$. If the adjacency matrix element $A_{ji} = 1$, then neuron i receives input from neuron j modeled by a Dirac delta function, which causes the voltage of neuron i to increase by S/N at each spike time τ_{jk} of neuron

j. Otherwise, $A_{ji} = 0$ and no input from the j^{th} neuron is received by neuron i. The numerical simulations we present are for an all-to-all coupled network with $A_{ij} = 1$ for all $i \neq j$, but the analysis we present is independent of the network structure. An event-driven algorithm is used to simulate the system described in Equation (2.1), similar to the one discussed in Sec. 2.4.1 of [9].

2.2. Synchronous oscillations. For the model described in Equation (2.1), network oscillations emerge when the excitatory coupling is large enough to synchronize the network through cascading firing events. A cascading firing event occurs when all neuron voltages are positioned sufficiently close to the firing threshold such that a spike from one neuron in the network is sufficient to induce firing in all other neurons in the network at that same time. Since all neurons spiked at the same time, their voltages are all reset to rest at the same time. Then, all neurons evolve (approximately) independently while their voltage remains pre-threshold, and the process repeats when one of the neurons' voltages reaches threshold again. Figure 2.1 shows two example networks that exhibit cascading events with different inter-event intervals. Assuming the voltage of each neuron evolves independently between each cascading event (since none of them are spiking), we can compute this time between firing events independently from the network structure and coupling strength [47–49].

Note that the synchronous cascading events do not occur periodically, but rather at random times governed by the time it takes the first neuron to reach the firing threshold and trigger a total cascading firing event. The oscillations can appear periodic as in Figure 2.1A, or sporadic as in Figure 2.1B, depending on the relative size of the variance to the mean of the random time between synchronous events. The power spectral densities (PSDs) in Figure 2.1 confirms the nearly periodic nature of the oscillations in Figure 2.1A, showing a concentrated peak near one frequency (along with the higher harmonics) in contrast to the lack of a peak frequency in Figure 2.1B. In general, quasi-periodic oscillations tend to arise in the presence of large external firing rates, as is the case in Figure 2.1.

In the remainder of this section, we calculate the mean time between synchronous firing events as a function of network parameters and use this calculation to predict which type of oscillations might arise, regular or sporadic. To begin, we consider the mean-driven regime in which the network neurons are driven over the threshold on average and have little variation in their firing times. Then, we consider the fluctuation-driven regime and compute the full distribution of the random time between synchronous events, which mathematically corresponds to the minimum first passage time of the collection of N independent voltages from V_R to V_T [47, 48]. In both cases, we employ a mean-dominated approximation of the Poisson spike train, taking a very large firing rate, $\nu \gg g_L$, and small strength, $f \ll g_L(V_T - V_R)$. We keep $f\nu \sim O(1)$ so that it takes many external spikes to enable a neuron's voltage to reach the threshold and the input can be approximated by Gaussian fluctuations around its mean drive.

2.2.1. Mean-driven network firing rate. In this section, we compute the mean time between synchronous firing events (the inverse of which is approximately the network firing rate) when the neurons are driven past threshold on average, i.e. the superthreshold regime. In this regime, the mean time between synchronous firing events can be approximated by the time it takes the voltage of the maximum of the N neuronal voltages to reach threshold, since this neuron will then excite all other neurons to spike as well, creating a synchronous event. The mean time between synchronous events is then computed by noting that no neurons fire in the time period between events when the network is in the perfectly-synchronous state, and thus all of the input to any given

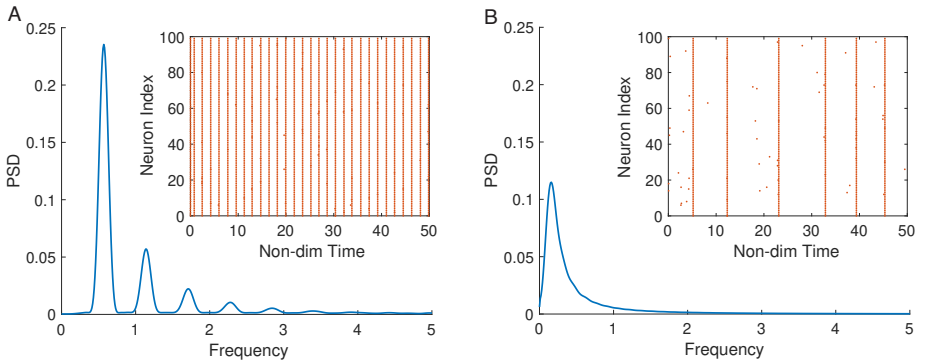

FIG. 2.1. *Power spectral density for two examples networks of excitatory current-based I&F neurons as described in Equation (2.1) with raster plot shown in the inset. (A) high external rate:* $f = 0.005, f\nu = 1.06$ *and* $S = 1.1$. *(B) low external rate:* $f = 0.005, f\nu = 0.86$ *and* $S = 1.1$.

neuron is only from the external spike train.

With the assumption that input is coming only from external sources, the solution to Equation (2.1) for the voltage of the i^{th} neuron during the time between events can be written as

$$v_i(t) = V_R + \sum_{l=1}^{M(t)} f e^{-g_L(t-s_{il})}, \tag{2.2}$$

ignoring the reset mechanism when the voltages reach threshold. The number of external spikes, $M(t)$, arriving at the i^{th} neuron before time t is random and Poisson-distributed with mean νt. Taking the mean-dominated approximation of the Poisson spike train for large ν, we arrive at an equation for the voltage in Equation (2.2) as a sum of a large number of independent random variables.

In [48] we used a central-limit argument to evaluate this random sum, showing that the PDF of the neuronal voltage, $v_i(t)$, which is not reset to V_R when it reaches threshold, is well approximated by the Gaussian PDF and corresponding CDF,

$$p_v(x,t) \sim \frac{1}{\sqrt{2\pi}\sigma(t)} \exp\left(-\frac{(x-\mu(t))^2}{2\sigma^2(t)}\right) \text{ and } F_v(x,t) \sim \frac{1}{2}\left[1 + \text{erf}\left(\frac{x-\mu(t)}{\sqrt{2}\sigma(t)}\right)\right], \tag{2.3a}$$

where $\text{erf}(z) = \frac{2}{\sqrt{\pi}} \int_0^z e^{-t^2}\, dt$ and the average voltage and variance are given by

$$\mu(t) = V_R + \frac{f\nu}{g_L}\left(1 - e^{-g_L t}\right) \quad \text{and} \quad \sigma^2(t) = \frac{f^2\nu}{2g_L}\left(1 - e^{-2g_L t}\right). \tag{2.3b}$$

Considering the N neuron voltages as independent between total synchronous events, the distribution of the maximal of the N voltages in the network is given by

$$p_v^{(N)}(x,t) = N p_v(x,t) F_v(x,t)^{N-1}. \tag{2.4}$$

Since we are operating in the superthreshold regime, one in which the neurons are driven past threshold on average, the standard deviation of the maximal neuronal voltage is small in comparison to the mean of its distribution, and the time τ when the first neuron

crosses threshold can be approximated by the deterministic time it takes for the average of the maximal voltage to reach threshold, i.e.,

$$V_T = \int_{-\infty}^{\infty} x p_v^{(N)}(x,\tau)dx. \tag{2.5}$$

Solving Equation (2.5) for τ, we obtain the firing rate of the network as τ^{-1}. This approximated firing rate is shown in Figure 2.2A as the black-dashed curve, which is a function of the average external drive, $f\nu$.

2.2.2. Fluctuation-driven network firing rate. The above calculation breaks down when Equation (2.5) has no solution, i.e. when the average maximum voltage never reaches the firing threshold. Even when Equation (2.5) has a solution, it can be a bad approximation for the mean time between firing events if the neuron behavior is driven by fluctuations in maximum voltage, rather than the average. This most noticeably happens in the subthreshold regime, a regime in which the neuronal voltages are just below the threshold on average and are only pushed above the threshold by a large fluctuation in the external input. In this section, we rework the calculation of the time between synchronous events by taking into account large fluctuations in the external drive.

Since the neurons still behave independently between synchronous firing events (few, if any, are firing), the time between synchronous firing events can be calculated as the minimum of N independent first-passage times for a single, uncoupled neuron voltage to reach threshold from rest. The PDF $p_T^{(1)}(t)$ of this minimum exit time $T^{(1)}$ is therefore given by

$$p_T^{(1)}(t) = N p_T(t)\Big(1 - F_T(t)\Big)^{N-1}, \tag{2.6}$$

where $p_T(t)$ is the PDF of a single neuron's exit time and $F_T(t) = \int_0^t p_T(t')dt'$ is the CDF. The expected time between total firing events is simply

$$\left\langle T^{(1)} \right\rangle = \int_0^{\infty} t p_T^{(1)}(t)dt, \tag{2.7}$$

and the network firing rate is approximately $\left\langle T^{(1)} \right\rangle^{-1}$.

To approximate the single-neuron exit time distribution, $p_T(t)$, we consider the evolution of a single neuron voltage that is removed from the system when its voltage reaches the threshold, i.e., it is "absorbed" at V_T. Then, the probability at time t that the neuron has not yet fired is the probability that it is still in the domain, $V_R \le x < V_T$. In [47, 48] we give a detailed treatment of computing this probability and subsequently the PDF, $p_T(t)$, and summarize the result here. With the mean-driven approximation of the Poisson process as Gaussian fluctuations about the mean, the evolution of a single neuron is approximately the solution to the following stochastic differential equation

$$dv = \left[-g_L(v - V_R) + f\nu\right]dt + f\sqrt{\nu}dW. \tag{2.8}$$

Then, the function $G(x,t)$ for the probability that the solution to Equation (2.8) has not yet crossed the threshold V_T given that it started at position x at time $t = 0$ satisfies the Kolmogorov Backwards Equation

$$\frac{\partial}{\partial t}G(x,t) = \Big[-g_L(x - V_R) + f\nu\Big]\frac{\partial}{\partial x}G(x,t) + \frac{f^2\nu}{2}\frac{\partial^2}{\partial x^2}G(x,t), \tag{2.9}$$

with the boundary and initial conditions $\frac{\partial}{\partial x}G(x,t)|_{x=V_R} = 0$, $G(V_T,t) = 0$ and $G(x,0) = 1$. We compute the $p_T(t)$ using a finite-difference approximation for the derivative of the CDF $F_T(t) = 1 - G(V_R,t)$, having solved system (2.9) numerically with the Crank-Nicolson scheme for $G(x,t)$.

The network firing rate, approximated by $\left\langle T^{(1)} \right\rangle^{-1}$, as a function of $f\nu$ is shown in Figure 2.2A, along with the network firing rate calculated in the previous section by solving Equation (2.5). Notice that this network firing rate found by taking the fluctuations into account is approximately equivalent to the mean-driven network firing rate, Equation (2.5), in the superthreshold regime ($f\nu > 1$) but begins to deviate significantly in the subthreshold regime ($f\nu < 1$). The corresponding PDFs of $p_T^{(1)}(t)$ in the superthreshold and subthreshold regimes are shown in Figure 2.2B. Notice that, in the superthreshold regime, the variance is small relative to its mean, creating oscillatory behavior seen in the raster plot in Figure 2.1A. In contrast, when this mean-driven assumption is no longer valid, e.g., in the subthreshold regime, the distribution $p_T^{(1)}(t)$ is wide, leading to scattered or intermittent firing that emerges from a quiescent state as in Figure 2.1B.

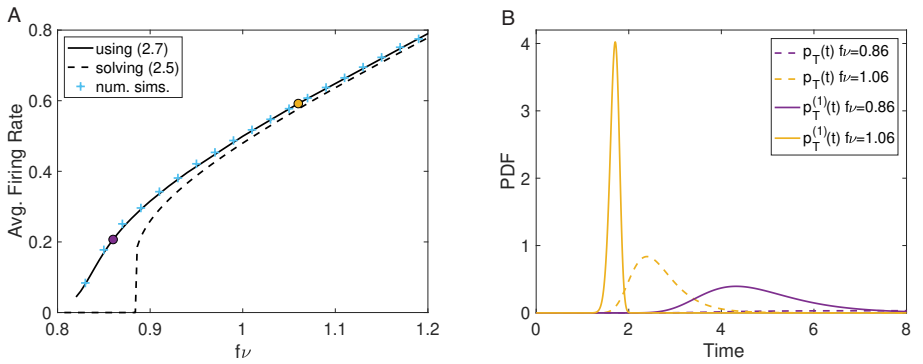

FIG. 2.2. *(A) The network firing rate as a function of mean external input (gain curve) computed for the synchronized network using the methods described in Sections 2.2.1 and 2.2.2. (B) For the two indicated points on the gain curve in (A), the single neuron first passage time distribution and minimum first passage time distribution are shown. For both panels,* $f = 0.005, N = 100$. *For the numerical simulations in (A), a value of* $S/N = 0.041$ *was chosen to ensure total synchronous events occur with high probability and the firing rate was averaged over a run of 800 non-dimensional time units.*

This all-excitatory network model has both an instantaneous response to spikes, as well as an instantaneous refractory period. Once a neuron has fired, its voltage is held at rest until the remainder of the cascading firing event has been resolved. Without this mechanism, due to the high coupling required for the network to exhibit total cascading firing events with high probability, the first neuron to fire in Figure 2.1A would receive enough input ($S(N-1)/N = 1.089 > V_T - V_R$) to fire again during a cascading firing event, perpetuating the cycle indefinitely. Realistically, neurons do not respond to spikes instantaneously and the refractory period has some finite length. In the next section, we implement a more realistic network model of conductance-based I&F neurons including both excitatory and inhibitory neurons, with realistic coupling probabilities and strengths, and non-instantaneous responses to spikes. With non-instantaneous responses, the cascading firing events observed in this section are no longer possible; however, the network still exhibits oscillatory behavior due to the

interaction between the inhibitory and excitatory neurons.

3. I&F excitatory and inhibitory network

One of the next simplest network models introduces conductance, rather than current, as the mode of communication between neurons, as well as the inclusion of inhibitory neurons, necessitating the expression of both an excitatory and inhibitory conductance. While still minimal, these anatomical and physiological assumptions are sufficient to reproduce experimentally-observed phenomena such as orientation selectivity and the line-motion illusion in large-scale modeling of the pinwheel structures in the primary visual cortex [57–59, 66]. In this section, we show that, with the inclusion of an additional inhibitory current with a slow time scale to mimic the effects of calcium currents, I&F neurons can reproduce the behavior of the insect olfactory bulb with odor-specific bound triplets of neurons [56].

In the insect olfactory bulb of the honeybee and locust, where odor input is initially processed, synchronized oscillations appear to emerge prominently in three stages. Upon receiving the stimulus from the olfactory receptor neurons, the olfactory-bulb network begins generating synchronized oscillations with a frequency of ~ 20 Hz [29,33,34]. These oscillations then subside for a period of time, after which the oscillations reemerge and modulate slowly (much less than 20 Hz) in a manner determined by the stimulus for about 1 second until they reach a steady state [76].

In this section, we show through simulations that one mechanism for the modulation of network oscillations in the olfactory bulb can be explained by the addition of a slow inhibitory conductance in the network I&F model neurons. We then coarse-grain this model into a time-varying firing-rate model and show that this coarse-grained model possesses a limit-cycle-like object in two of its variables, with the slow conductance variable directing the dynamics to undergo a slow passage through a saddle-point-on-a-circle bifurcation.

3.1. Model: Conductance-based I&F neurons. Similarly to Equation (2.1a), the voltage of the i^{th} neuron in the conductance-based I&F network is governed by

$$\tau \frac{dv_i}{dt} = -g_L\,(v_i - \varepsilon_R) - g_i^E(t)\,(v_i - \varepsilon_E) - g_i^F(t)\,(v_i - \varepsilon_F) - g_i^S(t)\,(v_i - \varepsilon_S)\,, \tag{3.1a}$$

for $i = 1, \ldots, N$. The voltage evolves according to Equation (3.1a) while $v_i < v_T$, and upon reaching v_T is immediately reset to ε_R. In this model, the current coming from network neurons are modeled through time-dependent excitatory, fast inhibitory, and slow inhibitory conductances, $g_i^E(t)$, $g_i^F(t)$, and $g_i^S(t)$, respectively. These conductances multiply the voltage difference from ε_R, ε_E, ε_F, and ε_S, which are the reversal potentials corresponding to leakage, excitatory, fast inhibitory, and slow inhibitory conductances, respectively, with the condition that $\varepsilon_S < \varepsilon_F < \varepsilon_R < V_T < \varepsilon_E$. A more detailed discussion of modeling the post-synaptic response to action potentials through the conductances can be found in [56].

Here, we summarize the modeling choice to include two inhibitory conductances. As shown in experiments [35] and more realistic models [3,53,54] (using HH neuron-models), the action potentials generated in olfactory neurons are prolonged due to voltage-gated calcium channels. Therefore, in this model, to capture the proper spike-timing due to calcium dynamics, we incorporate a fast inhibitory conductance, $g_i^F(t)$, with a decay constant that is larger than the typical value (4 ms vs. 1-2 ms) used in spiking neuron models. Additionally, experiments have determined the existence of a slow inhibitory current in insects such as the honeybee [2] and moth [43,44] and have seen evidence for

a similar current in the locust [35]. Therefore, we include a slow inhibitory conductance, $g_i^S(t)$, in a style similar to previous models [3, 53, 54].

Here, we summarize the modeling choice to include two inhibitory conductances. As shown in experiments [35] and more realistic models [3,53,54] (using HH neuron-models), the action potentials generated in olfactory neurons are prolonged due to voltage-gated calcium channels. In our I&F model we give up accurate modeling of the action potential and rather incorporate two inhibitory currents with adjusted time-scales to accurately capture the possible post-synaptic responses. The first, a fast inhibitory conductance, $g_i^F(t)$, has a decay constant that is larger than the typical value (4 ms vs. 1-2 ms) used in spiking neuron models. The second, a slow inhibitory conductance, $g_i^S(t)$, models experimentally observed slow responses to the calcium action potentials in insects such as the honeybee [2] and moth [43, 44] and possibly in the locust [35]. To exaggerate this slow response and mimic the overall insect spiking dynamics, we further lengthen the rise and decay time-scales (420 ms and 800 ms vs. 100 ms and 200 ms) of this post-synaptic response in comparison to previous models [3, 53, 54].

The excitatory, fast inhibitory, and slow inhibitory conductance responses for the i^{th} neuron are governed by

$$\sigma_P \frac{dg_i^P(t)}{dt} = -g_i^P(t) + h_i^P(t) \tag{3.1b}$$

$$\sigma_E \frac{dh_i^E(t)}{dt} = -h_i^E(t) + \frac{S_i^E}{N_E} \sum_{j \neq i} A_{ji}^E \sum_\mu \delta(t - t_\mu^j) + f_i \sum_k \delta(t - \tau_k^i) + f_i^{\text{or}} \sum_l \delta(t - \tau_l^i) \tag{3.1c}$$

$$\sigma_F \frac{dh_i^F(t)}{dt} = -h_i^F(t) + \frac{S_i^F}{N_I} \sum_{j \neq i} A_{ji}^F \sum_\mu \delta(t - t_\mu^j) \tag{3.1d}$$

$$\rho_S \frac{dh_i^S(t)}{dt} = -h_i^S(t) + \frac{S_i^S}{N_I} \sum_{j \neq i} A_{ji}^S \sum_\mu \delta(t - t_\mu^j), \tag{3.1e}$$

where $P = \{E, F, S\}$ and $\delta(\cdot)$ is the Dirac-delta function. The rise and decay times of the excitatory and fast inhibitory conductances are $\sigma_E = 1$ ms and $\sigma_F = 4$ ms. For the slow inhibitory conductance, we model a distinct rise time, $\rho_S = 420$ ms, and decay time, $\sigma_S = 800$ ms, to mimic the prolonged spike response. The synaptic connection strengths, denoted as S_i^E, S_i^F and S_i^S, take one of two values depending on the i^{th} neuron's type (E or I) and are scaled by the size of the corresponding population (N_E or N_I). The ratio of excitatory to inhibitory neurons in the network is kept constant at $N_E/N_I = 3$ [36]. The adjacency matrices A^E, A^F, and A^S are sparse, with the off-diagonal entries chosen randomly with the following probabilities: p_E^E and p_I^E for excitatory connections to excitatory and inhibitory neurons, respectively, p_E^F and p_E^S (p_I^F and p_I^S) for fast and slow inhibitory connections to excitatory (inhibitory) neurons.

Similar to Equation (2.1), Equation (3.1) also includes spikes of strength f_i arriving from a background external drive with arrival times, τ_k^i, generated by independent Poisson processes, all with the same rate ν. We allow for f_i to take one of two values, f_E or f_I, depending on the i^{th} neuron type (E or I). In addition, we model the presentation of an odor to about 1/3 of the neurons in the network with an additional set of external spikes of strength f_i^{or} at rate ν^{or}.

The model is normalized such that $\varepsilon_R = 0$, $\varepsilon_E = \frac{14}{3}$, $\varepsilon_F = -\frac{2}{3}$, $\varepsilon_S = -\frac{9}{5}$, and $V_T = 1$. We solve the model equations numerically using an algorithm developed by Shelly and Tao [63] for solving I&F neuron models accurately and efficiently.

3.2. PING oscillations. Our insect-olfaction model (3.1) produces oscillations with three similar stages of behavior as was observed experimentally. As shown in Figure 3.1A, initial oscillations (from 0 to 500 ms) are followed by a period of quiescence (from 500 ms to about 1500 ms), then slower oscillations arise (from 1500 ms to 2500 ms). The network oscillations emerge when the external input is sufficiently mean-driven such that many of the excitatory neurons arrive at threshold around the same time and slightly before the inhibitory neurons (external strength $f_E > f_I$). A majority of the excitatory neurons fire an action potential, exciting the inhibitory neurons to fire, which then, in turn, suppresses the excitatory neurons from firing for a period of time after the firing event. Once inhibition is released, the excitatory neurons again receive mean-dominated input that drives their voltages to the threshold, and the cycle repeats. This interaction between excitatory and inhibitory spiking is the fundamental principal underlying the pyramidal-interneuronal network gamma (PING) type oscillation [8, 77], which is thought to be the basis for many oscillations in the cortex, particularly those in the high-beta and gamma range [7]. This underlying PING mechanism between the excitatory and fast inhibitory conductances may explain the initial formation of fast oscillations observed in the olfactory bulb in response to the presentation of an odor, while slow inhibitory conductance modulates the frequency of these oscillations as the odor is processed.

The initial oscillations that arise during the first 300ms in Figure 3.1A can be reproduced using only excitatory and fast inhibitory conductances, as shown in the inset of Figure 3.1B, providing evidence that odor detection relies on the PING mechanism. Taking the PSD of the average voltage of the system shows that these oscillations occur at around 20Hz, as determined experimentally. Now, if we change the slow inhibitory conductances from zero to a fixed value of $g_i^S = 0.1$ for all neurons ($i = 1 \dots N$), we can reproduce the slow oscillations that emerge during the last 1000ms of Figure 3.1A, shown in the inset of Figure 3.1C. Notice that the peak in the PSD shifts to the left as the slow inhibition is turned on, see Figure 3.1C as compared to Figure 3.1B. We verify that the oscillations (at both frequencies) stem from cyclic dynamics between the inhibition and excitation in Figure 3.1D and E by plotting the average voltage of the excitatory and inhibitory neurons, as well as the excitatory fast inhibitory conductances. Next, we analyze a coarse-grained firing-rate model and show that these oscillatory dynamics are governed by a slow-conductance-modulated limit cycle, where large values of the slow conductance destroy the limit cycle (stop the initial 20Hz oscillations) and suppress neuronal firing (quiescent state).

3.3. Firing-rate model and limit cycle. To gain further mathematical insight into the existence and modulation of the oscillations, we coarse-grain the I&F model to a firing-rate model for the excitatory and inhibitory populations, writing equations for the four conductance variables: excitatory $g^E(t)$, fast inhibitory $g^F(t)$, slow inhibitory $g^S(t)$ and the intermediate variable $h^S(t)$. We assume for simplicity that the excitatory and fast conductances have infinitely fast rise times so that the secondary variables $h^E(t)$ and $h^F(t)$ are adiabatically eliminated. Then, the time-dependent neuronal firing rates, $m_E(t)$ and $m_I(t)$, for the excitatory and inhibitory populations, respectively, are derived in terms of these network conduction variables, which are then fed back into the evolution of the network conductance variables, closing the system.

We heuristically derive the firing-rate model with the following additional assumptions: (i) We are operating in the mean-driven regime, in which both network-generated and external-drive spikes are small and arrive at high rates. Then, summations over incoming spike trains become continuous functions representing the incoming firing rates.

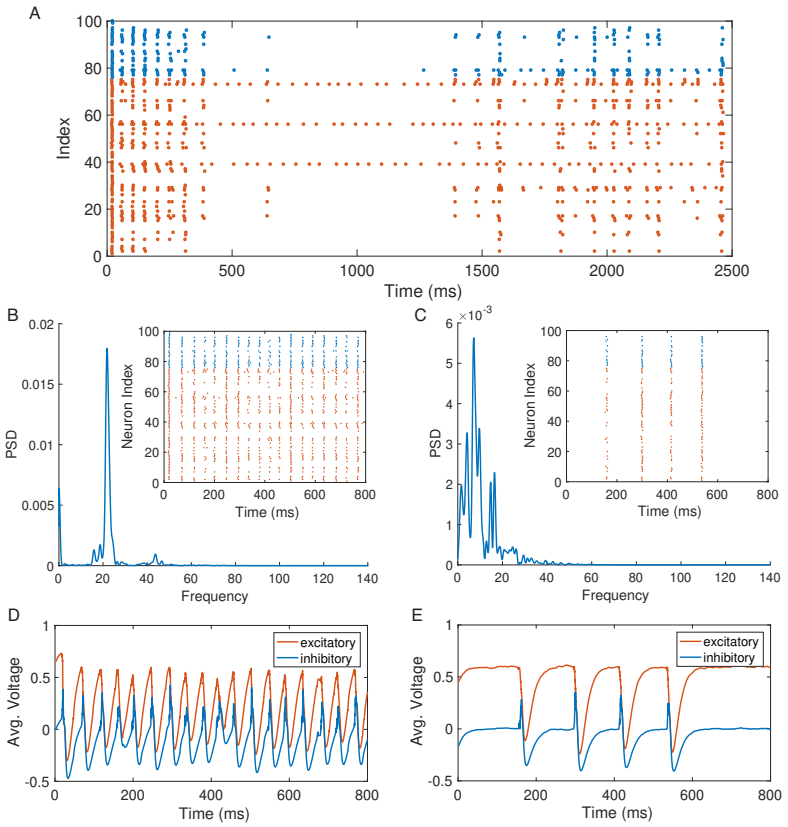

FIG. 3.1. *(A) Oscillations in the model of insect olfaction given by Equation (3.1). (B) PSD of the raster plot shown in the inset holding* $g_i^S = 0$ *for all neurons (C) PSD of the raster plot shown in the inset holding* $g_i^S = 0.1$ *for all neurons. (D)/(E) The average voltage for the excitatory and inhibitory populations corresponding to the raster plot in (B)/(C). In all panels the network size is* $N_E = 3N_I = 75$*, the time-scales are* $\sigma_E = 1ms$*,* $\sigma_F = 4ms$*,* $\rho = 420ms$*,* $\sigma_S = 800ms$*, the coupling strengths are* $S_E^E/N_E = 0.08$*,* $S_I^E/N_E = 0.315$*,* $S_E^F/N_I = 1.75$*,* $S_I^F/N_I = 0.35$*,* $S_E^S/N_I = 3.15$*,* $S_I^S/N_I = 0.63$*, the background drive rate is* $\nu = 4000Hz$ *with* $f_E\nu = 8$ *and* $f_I = 0$*, one third of the neurons are additionally driven with a rate of* $\nu^{or} = 6000Hz$*,* $f_E^{or}\nu^{or} = 6.9$*,* $f_I^{or}\nu^{or} = 6.6$ *to simulate the presentation of an odor, the network edges are randomly chosen with probabilities* $p_E^E = 2/15$*,* $p_I^E = 1/15$*,* $p_E^F = 0.15$*,* $p_I^F = 0.75$ *and the slow-conductance network is the same as the fast-conductance network in this case.*

(ii) Individual synaptic connections are replaced by the corresponding connection probabilities so that firing rates are scaled by the average number of connections. Together with the coupling strengths, the network drive terms are $S_i^E p_i^E m_E(t)$, $S_i^F p_i^F m_I(t)$, and $S_i^S p_i^S m_I(t)$. (iii) We assume $m_E(t)$ and $m_I(t)$ vary slowly in comparison to changes in the membrane potential and further speculate that the total conductance is very high, allowing us to treat the voltage in Equation (3.1) as a constant coefficient differential equation. We can then directly solve for the two population firing rates, $m_E(t)$ and $m_I(t)$, as the multiplicative inverses of the time for the corresponding voltage solutions to reach threshold from reset.

Under these assumptions, the evolution of the four network conductance variables

g^E, g^F, g^S, and h are given by

$$\sigma_E \frac{dg^E}{dt} = -g^E + m_E, \quad \sigma_F \frac{dg^F}{dt} = -g^F + m_I, \quad \sigma_S \frac{dg^S}{dt} = -g^S + h, \quad \rho_S \frac{dh}{dt} = -h + m_I, \tag{3.2a}$$

with m_E and m_I given by

$$m_Q(t) = \frac{1 + S_Q^E p_Q^E g^E + f_Q \nu + S_Q^F p_Q^F g^F + S_Q^S p_Q^S g^S}{\tau \ln[M_Q]}, \tag{3.2b}$$

where

$$M_Q = \frac{(S_Q^E p_Q^E g^E + f_Q \nu)(\varepsilon_E - \varepsilon_r) + S_Q^F p_Q^F g^F (\varepsilon_F - \varepsilon_r) + S_Q^S p_Q^S g^S (\varepsilon_S - \varepsilon_r)}{\left\{(\varepsilon_r - V_T) + \left(S_Q^E p_Q^E g^Q + f_Q \nu\right)(\varepsilon_E - V_T) + S_Q^F p_Q^F g^F (\varepsilon_F - V_T) + S_Q^S p_Q^S g^S (\varepsilon_S - V_T)\right\}^+}, \tag{3.2c}$$

with $Q \in \{E, I\}$. Here, $\{x\}^+ = x$ if $x > 0$ and zero otherwise. When the denominator in M_E (M_I) is zero, we define the corresponding firing rate m_E (m_I) to also be zero. Since the voltage and therefore the firing rate is driven by these conductance variables, we proceed to look for limit cycles in the $g^E - g^F$ plane as proxies for oscillations in the firing rates of the excitatory and inhibitory populations.

The dynamics of (3.2) shown in Figure 3.2A reproduces the three stages of the behavior of the full I&F model shown in Figure 3.1A. As before, we hold $g^S = 0$ constant to produce fast oscillations in the g^E and g^F variables (Figure 3.2B) and $g^S = 0.005$ constant to produce slower oscillations (Figure 3.2C). These oscillations are indeed limit cycles in the g^E-g^F plane, shown in Figure 3.2D, that shift downward with increasing g^S and lengthen their period as shown in Figure 3.2E. At about $g^S = 0.007$ the limit cycle hits the point $(0, 0)$ in the $g^E - g^F$ plane, the period goes to infinity, and a saddle-node-on-a-circle bifurcation occurs. The remaining stable fixed point is $(0, 0)$ corresponding to no firing. With g^S allowed to change as described by (3.2), the dynamics pass through this bifurcation point, only to return back through it producing oscillations at a slower rate; see Figure 3.2A.

Having shown that the PING oscillation modulated by a slow inhibitory conductance is sufficient to well-explain the mechanism underlying the three stages of oscillations in the insect olfactory bulb, we proceed in the next section to understand the effect of electrical coupling on the emergence of synchronous oscillations. Experimentalists have shown that electrical coupling exists between the pyramidal cells in the olfactory cortex of the Drosophilia and are essential in generating odor-specific synchronized patterns [78].

4. HH gap-junction network

One of the most realistic point-neuron models is the Hodgkin-Huxley (HH) neuron model, which can accurately describe the action potential of a spiking neuron in addition to the pre-threshold dynamics. In this section, we consider the oscillation-enhancing effects of direct electrical communication between neurons through sites called gap junctions (GJs) for those occurring between inhibitory interneurons, or "electrotonic" junctions (EJs) for those occurring between excitatory pyramidal cells [6, 16, 75]. Electrical junctions allow for the continuous flow of ions and small molecules between the connected cells, coupling the voltages of these cells through all stages of membrane depolarization. One implication is that an action potential in the pre-junctional cell will result in a quick rise in the voltage of the post-junctional cell almost instantaneously to the occurrence of the action potential. This event is called a spikelet and, together with the direct exchange of ions, is hypothesized to aid in synchronizing the network, though

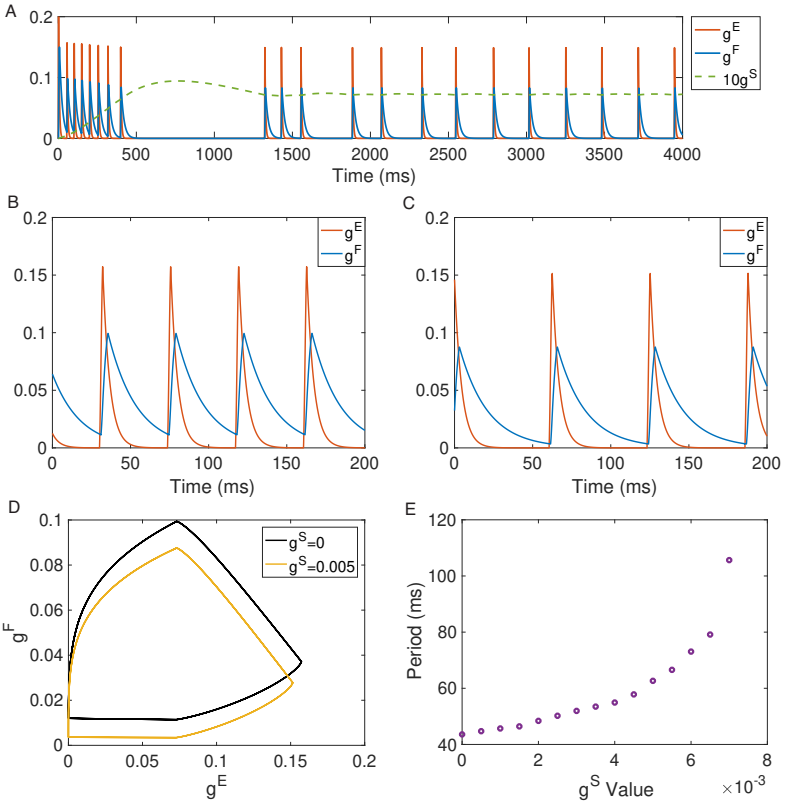

FIG. 3.2. *(A) Dynamics of the firing-rate model (3.2). (B) Dynamics of (3.2) with* $g^S = 0$ *held constant. (C) Dynamics of (3.2) with* $g^S = 0.005$ *held constant. (D) The same trajectories as (B) and (C) plotted in the 2-dimensional* $g^E - g^F$ *plane. (E) The period of the limit cycle as a function of* g^S *held constant. The remaining parameters are:* $\sigma_E = 4.5ms$, $\sigma_F = 18ms$, $\rho = 420ms$, $\sigma_S = 800ms$, $f_E\nu = 0.3$, $f_I\nu = 0.024$, $S_E^E p_E^E = 0.363$, $S_E^F p_E^F = S_E^S p_E^S = 4.995$, $S_I^E p_I^E = 0.45$, $S_I^F p_I^F = S_I^S p_I^S = 0.003$.

properties of this spikelet differ by neuron type and location. Interruption of the GJ electrical signaling between interneurons has been linked to diseases such as Ischemia and Alzheimer's Disease [17, 26], while computational studies suggest that EJ coupling between excitatory neurons may generate fast-frequency oscillations and play a role in inducing epileptic states [45, 67, 69].

In this section, we use a HH neuron model to show that the addition of GJ coupling among interneurons can promote the generation of synchronous oscillations, but the addition of EJ-coupling between excitatory neurons has little effect on global network properties. Then, we show that a coarse-grained version of the HH model, i.e., the I&F model, despite losing the ability to describe the voltage during an action potential, and therefore the details of a spikelet, is still capable of reproducing oscillation-enhancing effects when interneurons are coupled through weak, slow GJs.

4.1. Electrical coupling in cortex. Electrical junctions have been experimentally observed in several regions of the mammalian brain, most recently in the neocortex [41], and have been shown to exhibit different properties in each brain region. Even within one brain region, the various types of neurons may contain electrical

junctions with different properties.

One type of neuron called the fast-spiking (FS) interneuron, is one of the most ubiquitous inhibitory interneurons in the cortex [60] and has been shown to be widely coupled by gap junctions [30]. Experiments have determined that GJs occur between the dendrites of FS cells, occurring with a coupling probability of ~66% for cell distances of up to 80 μm [23, 24, 27]. The strength of the coupling, as determined by the ratio of the post-junctional voltage change in response to voltage changes in the pre-junctional cell (i.e., the coupling coefficient), is around 10%, with this coupling being bidirectional [23]. Experimentalists and computational neuroscientists have shown that GJ-coupling among these inhibitory neurons can be responsible for the generation and persistence of synchronous and oscillatory activity in the cortex [5, 15, 37, 65, 68] (for a review, see [41]), though for some coupling strengths, the inclusion of electric coupling can lead to asynchrony [25, 38].

In the hippocampus, neurons have been shown to contain electrical coupling between the axons of the pyramidal cells (PCs), or large excitatory cells responsible for projecting information to neurons in other layers. This coupling was measured to be extensive and large, forming a network of strongly-coupled excitatory cells [61]. This type of axo-axonal coupling has not been measured in the cortex; however, cortical cells have been shown to exhibit synchronized oscillations when GJs among interneurons are blocked, providing evidence for possible EJs among the cortical PCs [20, 42]. Only one experimentalist group has successfully measured several instances of EJ coupling between PCs in the cortex [75], though another experimentalist reported one potential EJ-coupled cortical pair as well [42]. The cortical EJs were measured to be rare, occurring only pair-wise between cells that have touching or overlapping cell bodies, with a coupling probability of 5% [75], and exhibiting nearly 25-times higher conductance strengths than GJs between FS cells. Moreover, action potentials in the pre-junctional cell were shown to elicit action potentials in the post-junctional cell with a probability of 50%, a property that has never been measured for GJ-coupled interneurons.

4.2. Model: HH Neurons. We model a network of cortical neurons using a modified version of the HH equations. Our modeling choice is motivated by the high conductance of the EJ, which strongly couples the membrane potentials of the pair of PCs at all times, including during an action potential, which requires us to accurately model the voltage during an action potential.

The voltage of the i^{th} HH neuron in the network is given by

$$\begin{aligned} C\frac{dv_i}{dt} = &- g_L(v_i - v_L) - \bar{g}_{Na}m^3h(v_i - v_{Na}) - \bar{g}_K n^4(v_i - v_K) \\ &- g_C\sum_j (v_i - v_j) - G_i^E(t)(v_i - v^E) - G_i^I(t)(v_i - v^I), \end{aligned} \tag{4.1}$$

where g_C is the electrical conductance, g_L is the leakage conductance, and $\bar{g}_{Na}$ and $\bar{g}_K$ are the maximal sodium and potassium conductances, respectively. The dynamics of the gating variables m, n, and h are described by $\frac{dx}{dt} = \alpha_x(v)(1-x) - \beta_x(v)x$, with $x = m, n, h$, where the voltage-dependent rate variables, $\alpha(v)$ and $\beta(v)$, are those defined in [55] for cortical regular-spiking and FS cells. The synaptic conductance, $G_i^Q(t)$ for $Q = \{E, I\}$, is modeled using smooth kinetics as described in Equations (16)-(21) in [64].

All parameters for this model are chosen to qualitatively match voltage clamp experiments for pairs of GJ-coupled FS cells (compared to experiments from [23]) and EJ-coupled PCs (compared to experiments from [75]). Specifically, for inhibitory neurons: $g_L = 0.1$ mS/cm^2, $V_L = -70$ mV, $\bar{g}_{Na} = 30$ mS/cm^2, $v_{Na} = 30$ mV, $\bar{g}_{Kd} = 5$

mS/cm^2, v_K = −90 mV, g_C = 0.012 mS/cm^2. For excitatory neurons: g_L = 0.025 mS/cm^2, V_L = −70 mV, $\bar{g}_{Na}$ = 60 mS/cm^2, v_{Na} = 55 mV, $\bar{g}_{Kd}$ = 3 mS/cm^2, v_K = −80 mV, g_C = 0.08 mS/cm^2. The reversal potentials for the synaptic currents are v^I = −80 mV and v^E = 0 mV. The network consists of 400 neurons including 25% FS cells and 75% PCs, on average [4]. The neurons are organized on a 20 × 20 grid with location-dependent, biologically-motivated connection probabilities and strengths for both the synaptic connections and electrical junctions. The probability of synaptic connectivity is location-dependent, decreasing exponentially with distance, as described in [40]. The electrical connectivity is also location dependent, with FS cells connecting to FS cells within a radius of ± 9 units with 50% probability, and PCs only connecting to neighboring PCs with 5% probability. All cells receive external input as described by a Poisson spike train with rate ν and strength F^Q, where $Q = \{E, I\}$. More details on the pairwise matching, as well as the network model parameters, can be found in [18].

4.3. Oscillations in a GJ-coupled network. Due to the ubiquitous GJ connectivity of the FS interneurons, the pre-threshold voltage of many interneurons is similar, leading to synchronized firing of those neurons when they receive sufficient excitation to spike. When a large portion of inhibitory neurons fire near the same time, a wave of inhibition is released into the network, leading to a suppression of activity for a short period after the initial wave of interneuron activity, thus leading to a synchronous network event. This mechanism is similar to the PING mechanism as described in the previous section, except that the inhibitory neurons are already synchronized pre-threshold when they receive excitation from the PC population, leading to a more synchronous event.

When the external drive is mean-dominated (large ν, small f in the external drive), the networks containing GJ coupling tend to exhibit oscillatory behavior, while the networks without GJ coupling, with and without EJ coupling, do not exhibit oscillations. Figure 4.1 shows raster plots and PSD plots for example networks containing no electrical coupling (no EC), GJ coupling, EJ coupling and both types of coupling (all EC). Notice that the PSD for the networks containing no electrical coupling and just EJ coupling are broad, with no clear peak frequency (Figure 4.1A and Figure 4.1C), while the networks containing GJ coupling have several peaks in their PSD plots (Figure 4.1B and Figure 4.1D), indicating oscillations are present in those networks containing GJ coupling.

To quantify the changes that occur in the network with the addition of each type of electrical coupling, we measure characteristics of the oscillations and network synchrony. These characteristics include the number of synchronous network events per second and the tightness of the synchrony exhibited in each event (termed the SD measure). To find the number of synchronous events per second, we count the number of times the average voltage of the network crosses a threshold, measuring the number of times a large portion of the network fires near the same time. Then, for each synchronous event, the SD measure calculates the width (standard deviation) of the distribution comprised of time differences from the event time to each neuron spike time within a window of ±20 ms of the event time. In this way, we observe that the SD measure determines the level of synchrony exhibited by all of the neurons that participate in each synchronous event, where low values indicate more tightly synchronized events. We observe that networks containing GJ coupling exhibit many more synchronous events than those networks that do not include GJ coupling, see Figure 4.2A, as expected from the raster plots in Figure 4.1. Additionally, each synchronous network event itself is more synchronized in the networks containing GJ coupling, as described by much lower SD values, than those

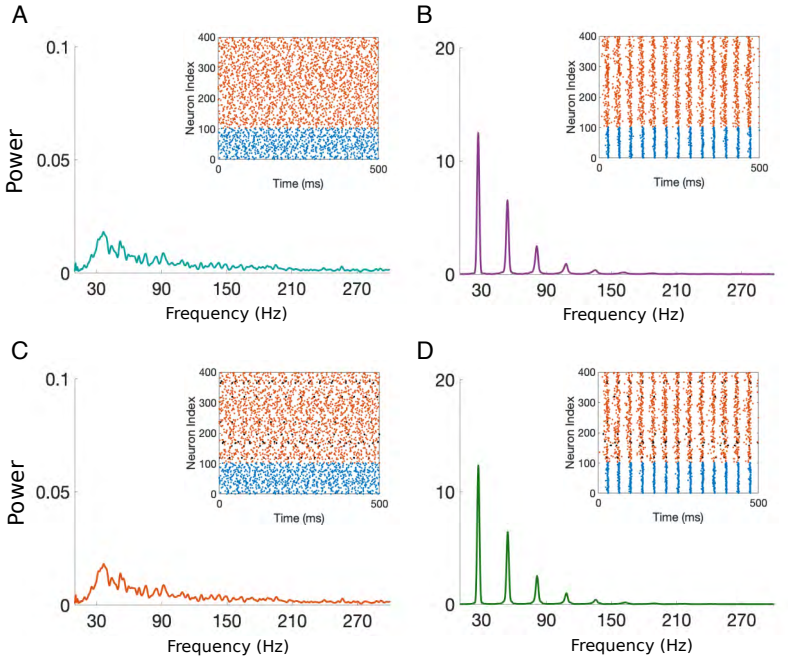

FIG. 4.1. *Example PSD plots with associated raster plots for HH networks containing different types of electrical coupling: (A) no electrical coupling (EC) , (B) GJ coupling, (C) EJ coupling , and (D) both GJ and EJ coupling (all EC). The black points represent the spike times of the neurons that are connected by an EJ. These simulations were run for an external rate of* $\nu = 8000$ *Hz, external strengths* $f^E = 0.23125$ mS/cm^2, $f^I = 0.4$ mS/cm^2, *and a simulation time of 10 seconds.*

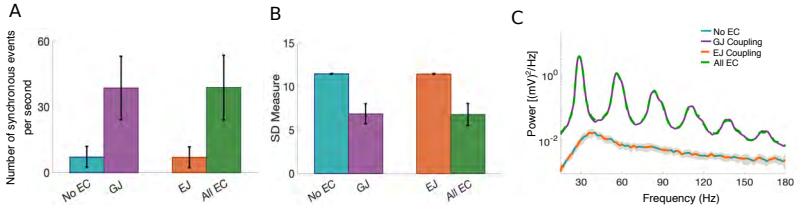

FIG. 4.2. *GJ coupling increases network synchrony and oscillations. (A) Number of synchronous events in the network. (B) The SD measure for all coupling regimes. (C) The PSD for all coupling regimes. All results are reported for 30 realizations of simulations run for 10 seconds of simulated time. The parameters are the same as in Figure 4.1 and the thresholds for determining synchronous events are -41 mV and -47 mV for networks containing GJ coupling and those not containing GJ coupling, respectively.*

networks without GJ coupling, see Figure 4.2B.

To uncover any network synchronizing effects of pair-wise EJ coupling, we measure characteristics of the PSD for the network containing GJ coupling and compare it to the network containing both EJ and GJ coupling (since networks without GJ coupling do not typically exhibit synchrony, we exclude those networks in this comparison). Figure 4.3A shows the frequency of the maximum peak in the PSD, the width of this maximum peak, and the height of this peak for both coupling regimes. Notice that the results are very similar, all within one standard deviation after averaging over 30 realizations.

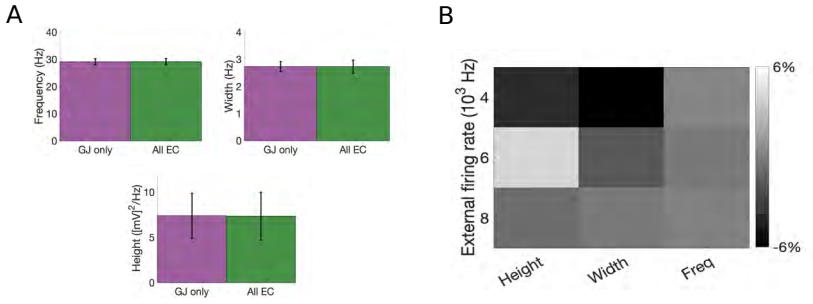

FIG. 4.3. *Comparing networks with GJ coupling and both GJ and EJ coupling. (A) Comparison of the frequency, width and height of the prominent peak in the PSD for the example network shown in 4.1. The error bars represent the standard deviation across 30 realizations of simulations each run for 10 seconds. (B) The average percent change (from GJ to all electric coupling (EC)) of each characteristic of the PSD for three different external input rate values,* $\nu = 4000, 6000, 8000$. *Note that* $f\nu$ *is held constant at* $f^E\nu = 1850$ *and* $f^I\nu = 3200$, *for all networks.*

The percent change in the mean, calculated from the network containing GJ coupling to both types of coupling, is shown in Figure 4.3B for each characteristic and over several different external rates, averaged over 30 realizations. Notice that the largest difference between these two networks is exhibited in the height of the prominent peak of the PSD for an external drive of 4000Hz, but that this difference is within one standard deviation and the percent change in the mean from the GJ coupling regime to the all-EC coupling regime is only 6%.

We have shown here, and in [18] in more detail, that the addition of GJ coupling between inhibitory neurons in cortical networks can aid in the formation of synchronous oscillations. The addition of rare, pairwise, strongly-coupled PCs does not significantly affect these oscillations, nor are they sufficient by themselves to create oscillations in a network without GJ coupling (recall Figure 4.1). However, with some network modifications, we show in [19] that the pair-wise synchrony induced by the EJ can lead to a network that has a large variability in its firing patterns and thus an increased coding capacity. Next, we coarse-grain this cortical HH model to the much more computationally-efficient I&F model and show that this coarse-grained model can capture the synchronizing properties of GJ coupling.

4.4. Coarse Graining HH. By coarse-graining the HH model (4.1) to an I&F model, of the form in Equation (3.1), we lose the ability to describe the voltage during an action potential. Despite this drawback, several modelers have successfully modeled the dynamics of a network containing GJ coupling using the I&F model. As we did in the HH model, the I&F model includes a term in the voltage equation describing the pre-threshold exchange of ions with the GJ-coupled cell (recall the $g_C \sum_j (v_i - v_j)$ term in Equation (4.1)). Since the I&F model does not resolve action potentials, this term alone will not result in spikelets in the post-junctional cell as it did for the HH model. As a fix, modelers have either included an instantaneous jump in the voltage of the post-junctional cell in response to a pre-junctional action potential [38, 51], or they have inserted a characteristic action potential/spikelet pair using a spiking kernel [14].

Since the GJ conductance is weak, and the resulting spikelet is small, for FS cells, we consider the approach that was taken by Patel and Joshi [52], which takes advantage of the slow time scale of dendro-dendritic GJs. This approach incorporates the average of the voltage of all pre-junctional cells, $\hat{v}_j$, over the last 50 ms rather than just the

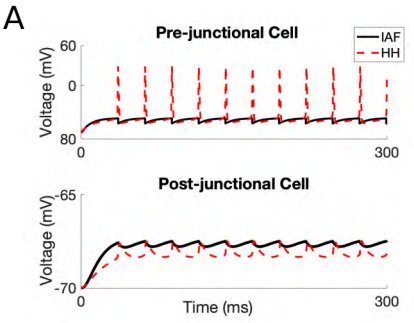

B

Parameter	FS Cells	PCs
g_L (mS/cm²)	0.045	0.01
g_C (mS/cm²)	0.012	0.0
ϵ_R (mV)	-70.0	-70.0
v_T (mV)	-49.3	-37.0
v_{reset} (mV)	-57.0	-50.0
C (μF/cm²)	1.0	1.0

FIG. 4.4. *Hodgkin-Huxley (HH) model of two GJ-coupled FS cells (red, dashed) plotted against the I&F model FS-cell GJ-coupled pair (black, solid) for one cell receiving a constant external input (pre-junctional, top) that is GJ-coupled with another FS cell receiving on external drive (post-junctional, bottom). Note that there is no synaptic coupling in this example. Parameters for this figure are as follows:* $I_{ext}^{I\&F} = 1.1\ \mu A$ *and* $I_{ext}^{I\&F} = 2.4\ \mu A$ *for the HH and I&F model, respectively.*

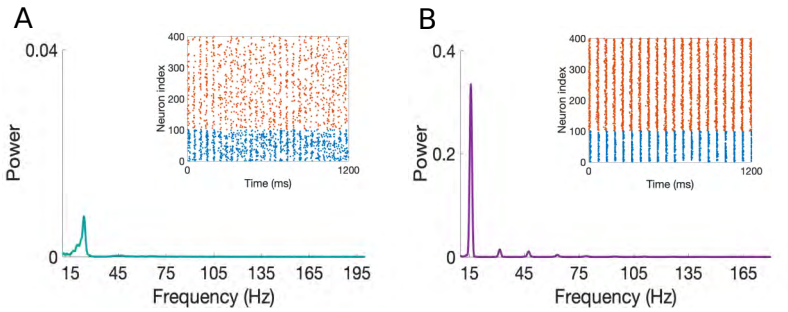

FIG. 4.5. *GJ coupling increases oscillations in I&F network. (A) PSD and associated raster plot for a network containing no electrical coupling, and (B) a network including GJ coupling. The parameters for this network can be found in Figure 4.4B.*

voltage of the post-junctional cell at time t. With this inclusion, the model system becomes

$$C\frac{dv_i}{dt} = -g_L(v_i - \epsilon_R) - g_i^E(t)(v_i - \epsilon^E) - g_i^I(t)(v_i - \epsilon^I) - g_C\sum_j(v_i - \hat{v}_j), \tag{4.2}$$

where $\hat{v}_j = \frac{1}{50}\int_{t-50}^{t} v_j(\tau)d\tau$ and the conductances are described as in Equations (3.1b) and (3.1c). We use this model to demonstrate that even these slow, dendro-dendritic GJs can enhance oscillations in a cortical network.

The parameters for this model are chosen such that the inhibitory and excitatory neurons behave similarly to those described by the HH model in the previous section, with particular attention paid to the GJ-coupled FS cells. Figure 4.4A shows a comparison of a pair of GJ-coupled FS cells in the HH model to a pair in the I&F model, with the parameters used to create this voltage plot shown in Figure 4.4B. Note that the post-junctional cell (bottom) as modeled by the HH model exhibits spikelets in response to action potentials in the pre-junctional cell (top), whereas the I&F model does not fully resolve those spikelets. Patel and Joshi showed how oscillations and synchrony arise in the Locus Coeruleus depending on the level of excitation in the network [52]. Here,

we simply demonstrate that the addition of these slow dendro-dendritic GJs among the FS cells can increase the power of oscillations in the network. Figure 4.5A shows the raster plot and PSD plot for the network containing only synaptic connections (no GJs) and Figure 4.5B shows those plots for the network containing GJs. Observe that the addition of GJ-coupling among FS cells increases the power of the 15Hz oscillation by more than a factor of 10.

It is exceedingly difficult to analytically study the HH model equations due to the severe nonlinearity necessary to describe the dynamics of the action potential. Non-spiking models such as the I&F model can be an adequate substitute when the communication between neurons is slow, occurring through synapses or dendro-dendritic gap junctions. Many modelers have shown through simulations that GJ-coupling can aid in oscillatory and synchronized behavior of neuronal networks, and yet others have shown through mathematical analysis the effect of changing the coupling strength on this network synchrony and oscillatory behavior [39]. In networks where the GJ coupling is strong and fast, I&F models need to include a term to model the spikelet (either through a spiking kernel or a delta function), whereas the HH model very accurately captures this spikelet without any additional modeling assumptions.

Additionally, in the HH model networks (see Figure 4.1), the addition of GJ coupling among the inhibitory cells can induce synchrony where there would be none without it due to the ability of the spikelets to drive the voltage of connected neurons over the firing threshold. In the I&F model with slow dendro-dendritic GJs, the presence of the GJs enhances the oscillations that are already present in the network, but their presence cannot create synchrony in networks that previously had none. However, I&F models are computationally efficient and easy to analyze, making them a good model when one's goal is to capture the global behavior of a network with slow GJs. As we have demonstrated here, the I&F model, with parameters chosen to mimic the cortical neurons described by the HH model, is sufficient to capture the enhancement of global oscillations that occurs due to GJ coupling among inhibitory cells.

5. Discussion

We have presented three models of neuronal networks that exhibit synchronous oscillations in the presence of noise. For each model, we identify three stages for the generation of oscillations that unify the underlying network mechanisms: (1) subthreshold dynamics, (2) initiating a firing event, and (3) synchronous termination of the event. In both I&F model networks, Equations (2.1) and (3.1), the mean-dominated external drive provides the mechanism for a majority of the subthreshold voltages to remain close to one another. In the HH network (4.1), GJs between the inhibitory neurons couples a large portion of the inhibitory network, resulting in similar subthreshold dynamics even in the presence of fluctuations in the external drive.

A synchronized firing event occurs when the spiking of a small portion of the excitatory neurons results in a majority of the network receiving enough excitation to be put over threshold and spike as well. In the all-excitatory network, this requires large coupling strengths and network connections to compensate for any differences in the subthreshold neuronal voltages. With the presence of inhibition in the I&F and the HH model, the excitatory neurons must arrive at the threshold slightly before the inhibitory neurons so that they may initiate a firing event. This may occur when the external drive to the excitatory neurons is slightly larger than the drive to the inhibitory neurons (I&F) or the net excitation is much larger for excitatory neurons than for inhibitory neurons (HH).

Oscillations will arise when this firing event is shut down, returning all neurons to a

similar starting point, and allowing the cycle to repeat. In the all-excitatory network, the instantaneous refractory period holds the neurons at rest until the majority of neurons in the network fire. In the networks containing inhibitory neurons, a wave of inhibition stops the firing event. In the HH model, this synchronized inhibition is enhanced by the GJ connectivity among the inhibitory neurons. Though the inhibitory neurons are less synchronized in the case of slow GJ connections due to the lack of spikelets, their presence is still sufficient to enhance oscillations that already existed in the network.

David Cai's insight was instrumental in guiding this work; his unique talent for seeking interesting questions, proposing new mathematical approaches, and fitting the pieces together to tell a cohesive story was rare and inspirational. His ingenuity and creativity in bringing theories and ideas from other disciplines to mathematical neuroscience has bettered and broadened the field, inspiring ourselves, as well as many others, to do the same.

REFERENCES

[1] V. Barranca, D. Johnson, J. Moyher, J. Sauppe, M. Shkarayev, G. Kovačič, and D. Cai, *Dynamics of the exponential integrate-and-fire model with slow currents and adaptation*, J. Comput. Neurosci., 37:161–180, 2014. 1

[2] G.S. Barbara, C. Zube, J. Rybak, M. Gauthier, B. Grunewald, *Acetylcholine, GABA and glutamate induce ionic currents in cultured antennal lobe neurons of the honeybee, Apis mellifera*, J. Comput. Physiol. A. Neuroethol. Sens. Neural. Behav. Physiol., 191:823–836, 2005. 3.1

[3] M. Bazhenov, M. Stopfer, M. Rabinovich, R. Huerta, H.D. Abarbanel, T.J. Sejnowski, and G. Laurent, *Model of transient oscillatory synchronization in the locust antennal lobe*, Neuron., 30:553–567, 2001. 1, 3.1

[4] C. Beaulieu, *Numerical data on neocortical neurons in adult rat, with special reference to the GABA population*, Brain Res., 609:284–292, 1993. 4.2

[5] M. Beierlein, J.R. Gibson, and B.W. Connors, *A network of electrically coupled interneurons drives synchronized inhibition in neocortex*, Nat. Neurosci., 3:904–910, 2000. 1, 4.1

[6] M.V.L. Bennett and R.S. Zukin, *Electrical coupling and neuronal synchronization in the mammalian brain*, Neuron., 41:495–511, 2004. 1, 4

[7] C. Borgers and N. Kopell, *Synchronization in networks of excitatory and inhibitory neurons with sparse, random connectivity*, Neural. Comput., 15:509–538, 2003. 3.2

[8] C. Borgers and N. Kopell, *Effects of noisy drive on rhythms in networks of excitatory and inhibitory neurons*, Neural. Comput., 17:557–608, 2005. 3.2

[9] R. Brette, M. Rudolph, T. Carnevale, M. Hines, D. Beeman, J.M. Bower, M. Diesmann, A. Morrison, P.H. Goodman, F.C. Harris Jr, M. Zirpe, T. Natschlager, D. Pecevski, B. Ermentrout, M. Djurfeldt, A. Lansner, O. Rochel, T. Vieville, E. Muller, A.P. Davison, S.E. Boustani, and A. Destexhe, *Simulation of networks of spiking neurons: A review of tools and strategies*, J. Comput. Neurosci., 23:349–398, 2007. 2.1

[10] A.N. Burkitt, *A review of the integrate-and-fire neuron model: I. homogeneous synaptic input*, Biol. Cybern., 95(2):97–112, 2006. 2

[11] G. Buzsaki and A. Draguhn, *Neuronal oscillations in cortical networks*, Science, 304:1926–1929, 2004. 1

[12] D. Cai, L. Tao, A.V. Rangan, and D.W. McLaughlin, *Kinetic theory for neuronal network dynamics*, Commun. Math. Sci., 4:97–127, 2006. 1

[13] D. Cai, L. Tao, M. Shelley, and D. McLaughlin, *An effective representation of fluctuation-driven neuronal networks with application to simple & complex cells in visual cortex*, Proc. Natl. Acad. Sci. USA, 101:7757–7762, 2004. 1

[14] C.C. Chow and N. Kopell, *Dynamics of spiking neurons with electrical coupling*, Neural. Comput., 12:1643–1678, 2000. 4.4

[15] B.W. Connors, *Synchrony and so much more: Diverse roles for electrical synapses in neural circuits*, Dev. Neurobiol., 77:610–624, 2017. 1, 4.1

[16] B.W. Connors and M.A. Long, *Electrical synapses in the mammalian brain*, Annu. Rev. Neurosci., 27:393–418, 2004. 4

[17] J.E. Contreras, H.A. Sanchez, L.P. Veliz, F.F. Bukauskas, M.V.L. Bennett, and J.C. Saez, *Role of connexin-based gap junction channels and hemichannels in ischemia-induced cell death in nervous tissue*, Brain Res. Rev., 47:290–303, 2004. 4

[18] J. Crodelle, G. Kovačič, D. Zhou, and D. Cai, *A computational model of electrotonic coupling between pyramidal cells*, submitted, 2019. 4.2, 4.3

[19] J. Crodelle, D. Zhou, G. Kovacic, and D. Cai, *A role for electrotonic coupling between cortical pyramidal cells*, Front. Comput. Neurosci., 13:33, 2019. 4.3

[20] E. Dere and A. Zlomuzica, *The role of gap junctions in the brain in health and disease*, Neurosci. Biobehav. Rev., 36:206–217, 2012. 4.1

[21] M.B. Feller, *Spontaneous correlated activity in developing neural circuits*, Neuron., 22:653–656, 1999. 1, 2

[22] N. Fourcaud-Trocmé, D. Hansel, C. van Vreeswijk, and N. Brunel, *How spike generation mechanisms determine the neuronal response to fluctuating inputs*, J. Neurosci., 23:11628–11640, 2003. 1

[23] M. Galarreta and S. Hestrin, *A network of fast-spiking cells in the neocortex connected by electrical synapses*, Nature, 402:72–75, 1999. 4.1, 4.2

[24] M. Galarreta and S. Hestrin, *Electrical synapses between GABA-releasing interneurons*, Nat. Rev. Neurosci., 2:425–433, 2001. 4.1

[25] J. Gao and P. Holmes, *On the dynamics of electrically-coupled neurons with inhibitory synapses*, J. Comput. Neurosci., 22:39–61, 2007. 4.1

[26] C. Giaume, J.C. Saez, W. Song, L. Leybaert, and C.C. Naus, *Connexins and pannexins in Alzheimer's disease*, Neurosci. Lett., 695(16):100–105, 2019. 4

[27] J.R. Gibson, M. Beierlein, and B.W. Connors, *Two networks of electrically coupled inhibitory neurons in neocortex*, Nature, 402:75–79, 1999. 4.1

[28] A. Giovanni, F. Capone, L. di Biase, F. Ferreri, L. Florio, A. Guerra, M. Marano, M. Paolucci, F. Ranieri, G. Salomone, M. Tombini, G. Thut, and V. Di Lazzaro, *Oscillatory activities in neurological disorders of elderly: Biomarkers to target for neuromodulation*, Front. Aging. Neurosci., 9:189, 2017. 1

[29] T. Heinbockel, P. Kloppenburg, and J.G. Hildebrand, *Pheromone-evoked potentials and oscillations in the antennal lobes of the sphinx moth Manduca sexta*, J. Comput. Physiol. A, 182:703–714, 1998. 1, 3

[30] S.G. Hormuzdi, M.A. Filippov, G. Mitropoulou, H. Monyer, and R. Bruzzone, *Electrical synapses: a dynamic signaling system that shapes the activity of neuronal networks*, Biochim. Biophys. Acta., 1662:113–137, 2004. 4.1

[31] W.M. Kistler, W. Gerstner, and J.L. van Hemmen, *Reduction of the Hodgkin-Huxley equations to a single-variable threshold model*, Neural. Comput., 9:1015–1045, 1997. 1

[32] G. Kovačič, L. Tao, A.V. Rangan, and D. Cai, *Fokker-planck description of conductance-based integrate-and-fire neuronal networks*, Phys. Rev. E, 80:021904, 2009. 1

[33] G. Laurent and H. Davidowitz, *Encoding of olfactory information with oscillating neural assemblies*, Science, 265:1872–1875, 1994. 1, 3

[34] G. Laurent, K.J. Seymour-Laurent, and K. Johnson, *Dendritic excitability and a voltage-gated calcium current in locust nonspiking local interneurons*, J. Neurophysiol., 69:1484–1498, 1993. 3

[35] G. Laurent, M. Wehr, and H. Davidowitz, *Temporal representations of odors in an olfactory network*, J. Neurosci., 16:3837–3847, 1996. 3.1

[36] B. Leitch and G. Laurent, *GABAergic synapses in the antennal lobe and mushroom body of the locust olfactory system*, J. Comput. Neurol., 372:487–514, 1996. 3.1

[37] T.J. Lewis and J. Rinzel, *Self-organized synchronous oscillations in a network of excitable cells coupled by gap junctions*, Network, 11:299–320, 2000. 4.1

[38] T.J. Lewis and J. Rinzel, *Dynamics of spiking neurons connected by both inhibitory and electrical coupling*, J. Comput. Neurosci., 14:283–309, 2003. 4.1, 4.4

[39] J.G. Mancilla, T.J. Lewis, D.J. Pinto, J. Rinzel, and B.W. Connors, *Synchronization of electrically coupled pairs of inhibitory interneurons in neocortex*, J. Neurosci., 27:2058–2073, 2007. 1, 4.4

[40] D. McLaughlin, R. Shapley, M. Shelley, and D.J. Wielaard, *A neuronal network model of macaque primary visual cortex (V1): orientation selectivity and dynamics in the input layer 4cα*, Proc. Natl. Acad. Sci. USA, 97:8087–8092, 2000. 4.2

[41] A. Mercer, *Electrically coupled excitatory neurones in cortical regions*, Brain Res., 1487:192–197, 2012. 4.1

[42] A. Mercer, A.P. Bannister, and A.M. Thomson, *Electrical coupling between pyramidal cells in adult cortical regions*, Brain Cell Biol., 35:13–27, 2006. 4.1

[43] A. Mercer, J.G. Hildebrand, *Developmental changes in the electrophysiological properties and response characteristics of Manduca antennal-lobe neurons*, J. Neurophysiol., 87:2650–2663, 2002. 3.1

[44] A. Mercer, J.G. Hildebrand, *Developmental changes in the density of ionic currents in antennal-lobe neurons of the sphinx moth, Manduca sexta*, J. Neurophysiol., 87:2664–2675, 2002. 3.1

[45] E. Munro and N. Kopell, *Subthreshold somatic voltage in neocortical pyramidal cells can control whether spikes propagate from the axonal plexus to axon terminals: a model study*, J. Neurophysiol., 107:2833–2852, 2012. 4

[46] W.H. Nesse, A. Borisyuk, and P.C. Bressloff, *Fluctuation-driven rhythmogenesis in an excitatory neuronal network with slow adaptation*, J. Comput. Neurosci., 25:317–333, 2008. 2

[47] K.A. Newhall, G. Kovačič, P.R. Kramer, and D. Cai, *Cascade-induced synchrony in stochastically-driven neuronal networks*, Phys. Rev. E, 82:041903, 2010. 2, 2.2, 2.2.2

[48] K.A. Newhall, G. Kovačič, P.R. Kramer, D. Zhou, A.V. Rangan, and D. Cai, *Dynamics of current-based, Poisson driven, integrate-and-fire neuronal networks*, Commun. Math. Sci., 8:541–600, 2010. 1, 2, 2.2, 2.2.1, 2.2.2

[49] K.A. Newhall, M.S. Shkarayev, P.R. Kramer, G. Kovačič, and D. Cai, *Synchrony in stochastically driven neuronal networks with complex topologies*, Phys. Rev. E, 91:052806, 2015. 2, 2.2

[50] M.J. O'Donovan, *The origin of spontaneous activity in developing networks of the vertebrate nervous system*, Curr. Opin. Neurobiol., 9:94–104, 1999. 2

[51] S. Ostojic, N. Brunel, and V. Hakim, *Synchronization properties of networks of electrically coupled neurons in the presence of noise and heterogeneities*, J. Comput. Neurosci., 26:369–392, 2009. 4.4

[52] M. Patel and B. Joshi, *Modeling the evolving oscillatory dynamics of the rat locus coeruleus through early infancy*, Brain Res., 1618:181–193, 2015. 4.4, 4.4

[53] M. Patel, A. Rangan, and D. Cai, *A large-scale model of the locust antennal lobe*, J. Comput. Neurosci., 27(3):553–567, 2009. 3.1

[54] M.J. Patel, A.V. Rangan, and D. Cai, *Coding of odors by temporal binding within a model network of the locust antennal lobe*, Front. Comput. Neurosci., 7:50, 2013. 3.1

[55] M. Pospischil, M. Toledo-Rodriguez, C. Monier, Z. Piwkowska, T. Bal, Y. Fregnac, H. Markram, and A. Destexhe, *Minimal Hodgkin-Huxley type models for different classes of cortical and thalamic neurons*, Biol. Cybern., 99:427–441, 2008. 4.2

[56] P.B. Pyzza, K.A. Newhall, D. Zhou, G. Kovačič, and D. Cai, *Network mechanism for insect olfaction*, submitted, arXiv:1908.11865, 2019. 3, 3.1

[57] A.V. Rangan, D. Cai, and D.W. McLaughlin, *Modeling the spatiotemporal cortical activity associated with the line-motion illusion in primary visual cortex*, Proc. Natl. Acad. Sci. USA, 102:18793–18800, 2005. 3

[58] A.V. Rangan, L. Tao, G. Kovačič, and D. Cai, *Large-scale computational modeling of the primary visual cortex*, in K. Josić, M. Matias, R. Romo, and J. Rubin (eds.), Coherent Behavior in Neuronal Networks, Springer Series in Comput. Neurosci., Springer-Verlag, 3:263–296, 2009. 1, 3

[59] A.V. Rangan, L. Tao, G. Kovačič, and D. Cai, *Multi-scale modeling of the primary visual cortex*, IEEE Eng. Med. Biol. Mag., 28:19–24, 2009. 3

[60] B. Rudy, G. Fishell, S. Lee, and J. Hjerling-Leffler, *Three groups of interneurons account for nearly 100% of neocortical GABAergic neurons*, Dev. Neurobiol., 71:45–61, 2011. 4.1

[61] D. Schmitz, S. Schuchmann, A. Fisahn, A. Draguhn, E.H. Buhl, E. Petrasch-Parwez, R. Dermietzel, U. Heinemann, and R.D. Traub, *Axo-axonal coupling. a novel mechanism for ultrafast neuronal communication*, Neuron., 31:831–840, 2001. 4.1

[62] M. Shelley and D. McLaughlin, *Coarse-grained reduction and analysis of a network model of cortical response. I. drifting grating stimuli*, J. Comput. Neurosci., 12:97–122, 2002. 1

[63] M. Shelley and L. Tao, *Efficient and accurate time-stepping schemes for integrate-and-fire neuronal networks*, J. Comput. Neurosci., 11:111–119, 2001. 3.1

[64] Y. Sun, D. Zhou, A.V. Rangan, and D. Cai, *Pseudo-Lyapunov exponents and predictability of Hodgkin-Huxley neuronal network dynamics*, J. Comput. Neurosci., 28:247–266, 2010. 4.2

[65] G. Tamas, E.H. Buhl, A. Lorincz, and P. Somogyi, *Proximally targeted GABAergic synapses and gap junctions synchronize cortical interneurons*, Nat. Neurosci., 3:366–371, 2000. 1, 4.1

[66] L. Tao, D. Cai, D.W. McLaughlin, M.J. Shelley, and R. Shapley, *Orientation selectivity in visual cortex by fluctuation-controlled criticality*, Proc. Natl. Acad. Sci. USA, 103:12911–12916, 2006. 3

[67] R.D. Traub, M.O. Cunningham, T. Gloveli, F.E.N. LeBeau, A. Bibbig, E.H. Buhl, and M.A. Whittington, *GABA-enhanced collective behavior in neuronal axons underlies persistent gamma-frequency oscillations*, Proc. Natl. Acad. Sci. USA, 100:11047–11052, 2003. 1, 4

[68] R.D. Traub, N. Kopell, A. Bibbig, E.H. Buhl, F.E. LeBeau, and M.A. Whittington, *Gap junctions between interneuron dendrites can enhance synchrony of gamma oscillations in distributed networks*, J. Neurosci., 21:9478–9486, 2001. 4.1

[69] R. D. Traub, I. Pais, A. Bibbig, F.E.N. LeBeau, E.H. Buhl, S.G. Hormuzdi, H. Monyer, and M.A. Whittington, *Contrasting roles of axonal (pyramidal cell) and dendritic (interneuron) electrical coupling in the generation of neuronal network oscillations*, Proc. Natl. Acad. Sci.

USA, 100:1370–1374, 2003. 4

[70] A. Treves, *Mean field analysis of neuronal spike dynamics*, Network, 4:259–284, 1993. 1

[71] H. C. Tuckwell, *Introduction to Theoretical Neurobiology: Volume 2, Nonlinear and Stochastic Theories*, Cambridge Studies in Mathematical Biology, Cambridge University Press, 1988. 2

[72] C. van Vreeswijk and D. Hansel, *Patterns of synchrony in neural networks with spike adaptation*, Neural. Comput., 13:959–992, 2001. 2

[73] B.B. Vladimirski, J. Tabak, M.J. O'Donovan, and J. Rinzel, *Episodic activity in a heterogeneous excitatory network, from spiking neurons to mean field*, J. Comput. Neurosci., 25:39–63, 2008. 2

[74] X.J. Wang and G. Buzsaki, *Gamma oscillation by synaptic inhibition in a hippocampal interneuronal network model*, J. Neurosci., 16:6402–6413, 1996. 1

[75] Y. Wang, A. Barakat, and H. Zhou, *Electrotonic coupling between pyramidal neurons in the neocortex*, PLoS One, 5:e10253, 2010. 4, 4.1, 4.2

[76] M. Wehr and G. Laurent, *Odour encoding by temporal sequences of firing in oscillating neural assemblies*, Nature, 384:162–166, 1996. 3

[77] M.A. Whittington, R.D. Traub, N. Kopell, G.B. Ermentrout, and E.H. Buhl, *Inhibition-based rhythms: experimental and mathematical observations on network dynamics*, Int. J. Psychophysiol., 38:315–336, 2000. 3.2

[78] R.I. Wilson, *Early olfactory processing in Drosophila: mechanisms and principles*, Annu. Rev. Neurosci., 36:217–241, 2013. 3.3

[79] G.G. Yener and E. Basar, *Brain oscillations as biomarkers in neuropsychiatric disorders: following an interactive panel discussion and synopsis*, Suppl. Clin. Neurophysiol., 62:343–363, 2013. 1